

Efficient multi-level hp -finite elements in arbitrary dimensions

Philipp Kopp^{*1}, Ernst Rank^{2, 3}, Victor M. Calo⁴ and Stefan Kollmannsberger¹

¹Chair of Computational Modeling and Simulation, Technische Universität München

²Chair for Computation in Engineering, Technische Universität München

³Institute for Advanced Study, Technische Universität München

⁴Applied Mathematics, School of Electrical Engineering, Computing & Mathematical Science, Faculty of Science and Engineering, Curtin University

Abstract

We present an efficient algorithmic framework for constructing multi-level hp -bases that uses a data-oriented approach that easily extends to any number of dimensions and provides a natural framework for performance-optimized implementations. We only operate on the bounding faces of finite elements without considering their lower-dimensional topological features and demonstrate the potential of the presented methods using a newly written open-source library. First, we analyze a Fichera corner and show that the framework does not increase runtime and memory consumption when compared against the classical p -version of the finite element method. Then, we compute a transient example with dynamic refinement and derefinement, where we also obtain the expected convergence rates and excellent performance in computing time and memory usage.

Keywords: high-order finite elements, hp -refinement, arbitrary hanging nodes

1. Introduction

For smooth solutions, p -finite element methods converge exponentially with respect to the number of unknowns [1]; for rough solutions, hp -finite elements recover the exponential convergence [2] where element sizes and polynomial degrees gradually decrease towards the solution singularities. The decision of whether to refine h or p can be automated by combining an error estimator and a smoothness indicator (see, e.g., [3, 4]). Classical implementations of hp -finite element methods follow a refinement by replacement strategy [5], in which smaller elements substitute elements marked to be refined. Once the new mesh is constructed, the shape functions of the smaller elements must be connected to the shape functions of neighboring elements in a non-trivial way to obtain a globally C^0 continuous finite element basis. In particular, the richer space of the fine elements must be constrained to the coarse shape functions of the neighbors. Especially in regions with sharp transitions between coarse and fine elements, these constraints introduce complicated dependencies on already constrained elements.

We follow the multi-level hp -method introduced in [6, 7] that simplifies the construction of hp -bases using a refine-by-superposition approach rather than a refinement-by-replacement. This superposition defines shape functions on all levels of the refinement tree and simplifies the construction of compatible basis functions significantly. The original framework [6, 7] builds an object-oriented data structure to store the various topological relations between the elements and their sub-topologies (faces, edges, nodes in three dimensions). Then, basis functions are associated to topological components, which allows the formulation of two rules for constructing multi-level hp -bases.

^{*}philipp.kopp@tum.de, Corresponding author

Motivated by the simplicity of the method, we extend the framework to four dimensions to allow conforming space-time discretizations of transient three-dimensional problems. The application in space-time discretizations of parabolic problems follows in a separate publication. Here, we focus on extending the multi-level hp -method to higher dimensions. While being convenient, the original object-oriented data structure becomes increasingly complex with each new dimension. The classical multi-level hp approach in four dimensions constructs objects for each 4-cube and its eight cubes, twenty-four faces, thirty-two edges, and sixteen nodes. Each topological entity lists its adjacent finite elements (4-cubes) and its overlay topologies (e.g., faces may list four overlay faces) and its topological elements (e.g., faces list their four edges and four nodes, while edge list their two nodes).

The number of dependencies in such a data structure consumes a significant amount of memory while being tedious to construct and maintain. Herein, we introduce a data-oriented alternative. While the basis functions are identical, we only require basic topological relations between cells in the refinement tree, not their lower-dimensional bounding topologies. Using these basic relations, we introduce a four-step algorithm to construct a d -dimensional mask of Boolean values; this tensor-product mask activates the proper shape functions from the entire tensor-product space of integrated Legendre shape functions leaving the others inactive. We construct location maps that combine the active shape functions on each element to the globally compatible hp -basis functions. By storing all the data in array-type containers, the effort of implementing a sophisticated object-oriented data structure becomes developing a capable low-level implementation of these containers. NumPy has been a significant influence on the ideas presented here. Moreover, we want to mention [8] as an approach that relates closely to our work.

Throughout this paper, we use the linear heat equation as a model problem:

$$\begin{aligned} \nabla \cdot (\kappa \nabla u) &= f & \text{on } \Omega \\ u &= u_d & \text{on } \Gamma_D \\ \kappa \nabla u \cdot n &= h & \text{on } \Gamma_N, \end{aligned} \tag{1}$$

where $\Gamma_D \cap \Gamma_N = \partial\Omega$ and $\Gamma_D \cup \Gamma_N = \emptyset$. The weak form of (1) reads as follows: Find $u \in u_d + \mathcal{H}_0^1(\Omega)$, such that

$$\int_{\Omega} \nabla w \cdot \kappa \nabla u \, d\Omega = \int_{\Omega} w f \, d\Omega + \int_{\Gamma_N} w h \, d\Gamma_N \quad \forall w \in \mathcal{H}_0^1(\Omega).$$

We assume that we can mesh Ω using a Cartesian grid, which is not a restriction of the method but results from the lack of robust mesh generators for higher-order methods. Despite the significant effort in the past [9–11], presently, we have no robust mesh generators producing boundary conforming finite elements for higher-order polynomials for arbitrary geometries in three dimensions. A common approach for complicated cases is to use immersed techniques [1, 12, 13] that use non-conforming (Cartesian) grids. The influence from outside of the physical domain is then minimized in the numerical integration of the element stiffness matrices, such that accuracies comparable to boundary conforming discretizations can be achieved.

This paper is structured as follows. In Section 2, we introduce a data structure for space-tree-based partitions of Ω . We then discuss the integrated Legendre shape functions and their tensor-product in higher dimensions in Section 3. To enable selectively deactivating them on each cell of the refinement tree, we introduce a *tensor-product mask*. Section 4 introduces the algorithm to construct a multi-level hp -basis based on the data structure described before. In Section 5, we verify the algorithms and their implementation on a set of examples and show that they behave as expected.

2. Hierarchical mesh partition and data structure

We first create a (Cartesian) base mesh on Ω . The h -refinement process follows this step, where cells marked for refinement are overlaid by 2^d sub-cells from bisecting the original cell in each coordinate direction. Performing this process recursively on overlay cells yields a 2^d -ary refinement tree. All cells within this tree can support basis functions, although we choose finite elements only as leaf cells. A central aspect of our framework is to identify a lightweight data structure that can store all essential information for constructing an hp -basis. This section details the data needed for the algorithms we

present in Section 4; although additional information, for example, the geometric mapping function of each cell, needs to be added on top.

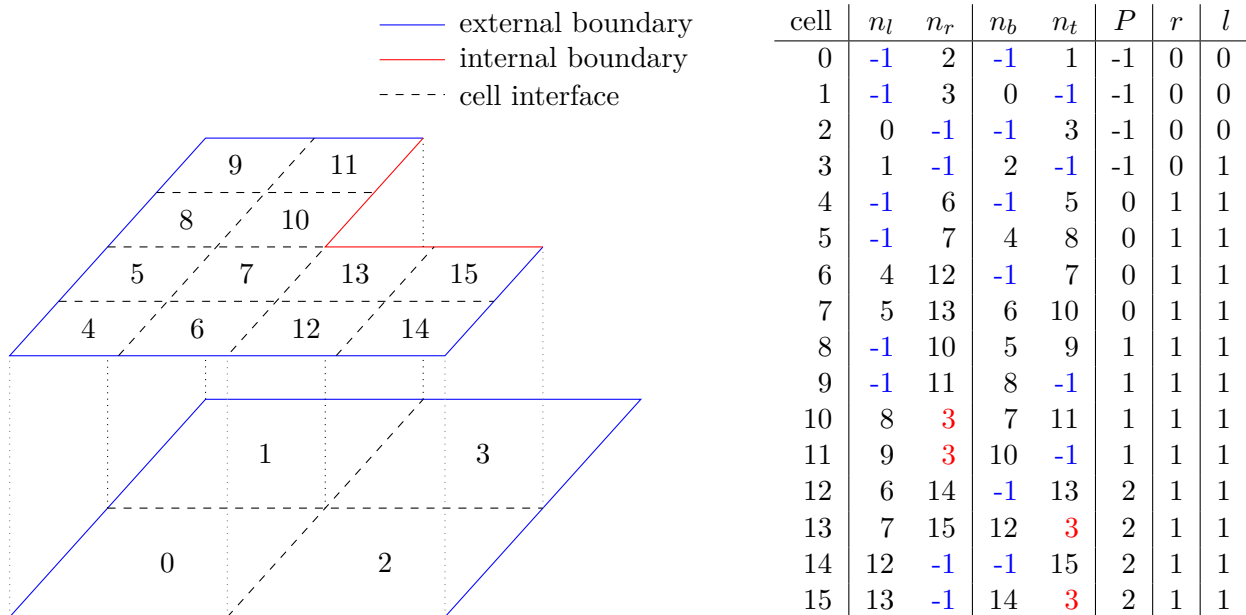


Figure 1. Essential topological information for each cell: Left and right neighbors n_l and n_r , bottom and top neighbors n_b and n_t , parent index P , refinement level r , and a Boolean value l indicating whether the cell is a leaf (*i.e.*, finite element) or not.

The essential topological relations are the parent, the refinement level, the neighbors of each cell, and whether a cell is a leaf. We store the parent information as an array of cell indices with one entry per cell. If a cell does not have a parent, we use a dedicated *no cell* value; for example, -1 for signed integers or the maximum representable number for unsigned integers. The cell indices are unique numbers assigned to each cell in the refinement tree. This number is not explicitly stored but rather represents the index of the cell in the data arrays. We store the neighbor information for each cell in an $(n, d, 2)$ sized array containing the indices of the next cell among the two boundaries in each coordinate direction. Here, we distinguish between *external boundaries* (no neighbor), *internal boundaries* (neighbor of lower refinement level), and *cell interfaces* (neighbor of same refinement level). Within the neighbor array, we assign the *no cell* value for *external boundaries* and the index of the most refined coarser neighbor for *internal boundaries*. Figure 1 sketches a simple example mesh with one level of refinement. On an *internal boundary*, the finer cell connects to the coarser cell, but the coarser cell connects to a base cell of its finer neighbor.

Having the refinement level of each cell available allows distinguishing between *internal boundaries* (neighbor has lower refinement level) and *cell interfaces* (neighbor has same refinement level). A list of Boolean values indicating whether a cell is a leaf or not is then required to assign the initial tensor-product masks in the first step of the algorithm introduced in Section 4.1. We tailor this data structure for the algorithms of Section 4, but one can exploit that much of the redundant information in our code does not need to be stored permanently.

3. Integrated Legendre shape functions

After establishing the geometric subdivision of Ω , we then introduce the shape functions on a reference coordinate system. The integrated Legendre polynomials on $r \in [-1, 1]$ are as follows:

$$I_0(r) = \frac{1}{2}(1-r) \quad I_1(r) = \frac{1}{2}(1+r) \quad I_q(r) = \frac{L_q(r) - L_{q-2}(r)}{\sqrt{4q-2}} \quad \text{for } q > 1, \quad (2a)$$

$$I'_0(r) = -\frac{1}{2} \quad I'_1(r) = \frac{1}{2} \quad I'_q(r) = \frac{L'_q(r) - L'_{q-2}(r)}{\sqrt{4q-2}} \quad \text{for } q > 1, \quad (2b)$$

where $L_q(r)$ are the Legendre polynomials of degree q :

$$L_0(r) = 1 \quad L_1(r) = r \quad L_q(r) = \frac{2q-1}{q}r L_{q-1} - \frac{q-1}{q}L_{q-2} \quad \text{for } q > 1, \quad (3a)$$

$$L'_0(r) = 0 \quad L'_1(r) = 1 \quad L'_q(r) = \frac{2q-1}{q}(L_{q-1} + rL'_{q-1}) - \frac{q-1}{q}L'_{q-2} \quad \text{for } q > 1. \quad (3b)$$

The hierarchical nature of this basis yields the important property that the basis $\{I_0, \dots, I_p\}$ for $\mathcal{P}_p([-1, 1])$ can be extended to form a basis for $\mathcal{P}_{p+1}([-1, 1])$ by simply adding the function I_{p+1} . Another important property is that I_0 is the only non-zero function on the left boundary. Similarly, I_1 is the only non-zero function on the right boundary, which allows us to classify the functions into left and right nodal modes (I_0 and I_1) and internal modes (I_p , if $p \geq 2$) (bubbles). Figure 2 shows

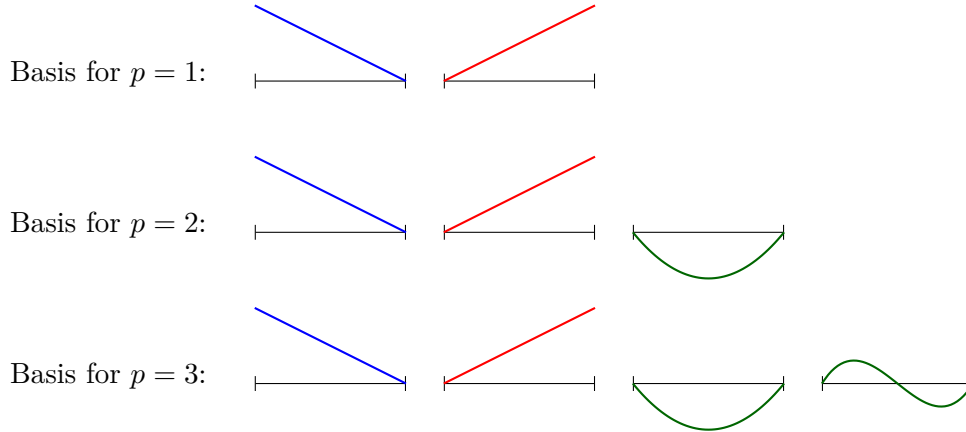


Figure 2. One-dimensional Integrated Legendre shape functions.

the integrated Legendre bases for $p = 1 - 3$.

In higher dimensions, we define an integrated Legendre basis in each coordinate direction as: $\{I_0, \dots, I_{p_i}\}$. The polynomial degrees in different coordinate axes may vary; thus, p is now a tuple (p_0, \dots, p_{d-1}) with a possibly different polynomial degree per axis. Now, a basis for the tensor-product space can be defined as follows:

$$\left\{ N_\alpha(r) = I_{\alpha_0}(r_0) \cdot I_{\alpha_1}(r_1) \cdot \dots \cdot I_{\alpha_{d-1}}(r_{d-1}) \mid \text{for } \alpha \in \{0, \dots, p_0\} \times \dots \times \{0, \dots, p_{d-1}\} \right\}, \quad (4)$$

where r_i are the local coordinates in direction i , and each $\alpha_i \in \{0, \dots, p_i\}$ indexes the one-dimensional shape functions in direction i . In two dimensions, for example, (4) becomes

$$\left\{ N_{ij}(r_0, r_1) = I_i(r_0) \cdot I_j(r_1) \mid \text{for } i \in \{0, \dots, p_0\}, j \in \{0, \dots, p_1\} \right\},$$

where r_0 and r_1 are the two local coordinates. Figure 3 displays the basis functions in (4) for $p = (3, 2)$. Independent of the polynomial degree, we identify rows for the functions with support on the left and right boundaries and columns for the functions with support on the bottom and top

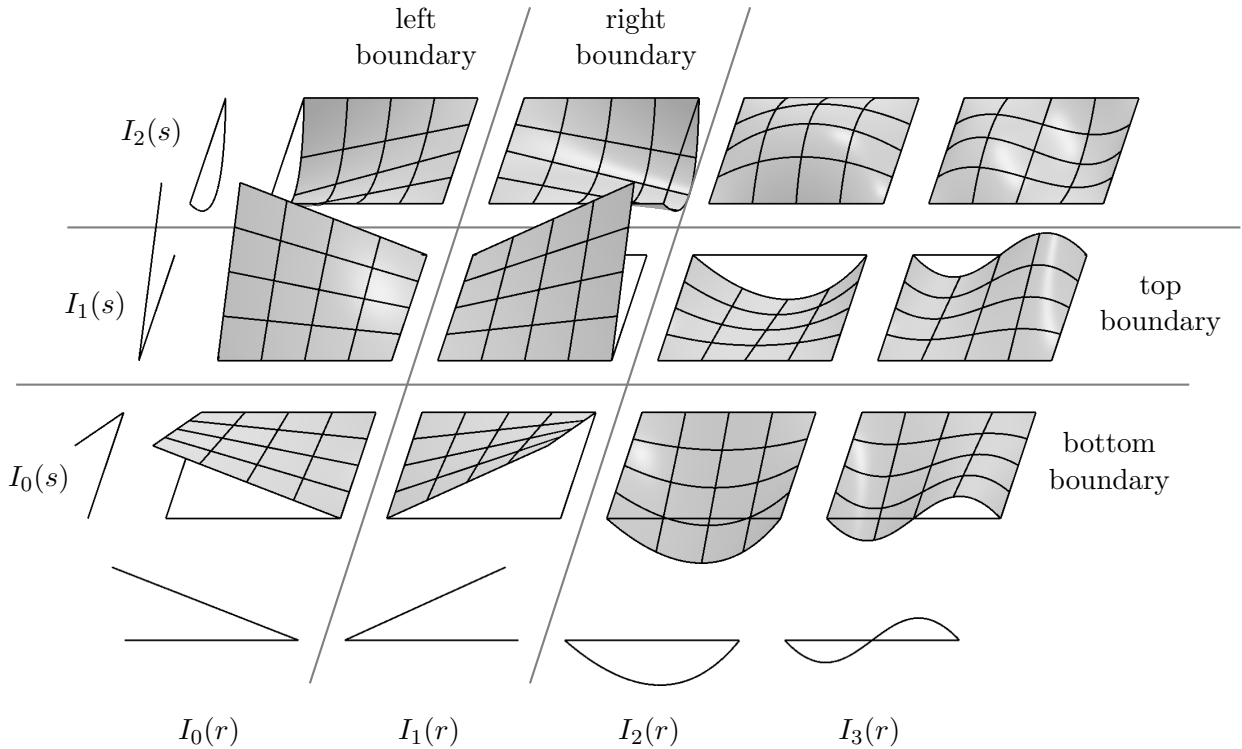


Figure 3. Tensor-product of Integrated Legendre shape functions for $p = (3, 2)$.

boundaries. This structure allows imposing zero Dirichlet conditions on the boundary of a cell by simply deactivating (removing) the respective row or column from the tensor-product.

This concept translates easily to higher dimensions, where we associate a $d - 1$ dimensional slice of the tensor-product to each boundary of a cell. In three dimensions, we have a two-dimensional slice for each of the six boundaries; in four dimensions, we have a three-dimensional slice for each of the eight boundaries, and so on. In general, we have two boundaries with a corresponding slice for each coordinate axis. We identify each slice by its normal axis and the index along this axis within the tensor-product (either 0 or 1). For example, in two dimensions, $(0, 1)$ corresponds to the right boundary slice, which is normal to axis zero at index one, and $(1, 0)$ corresponds to the bottom boundary, which is normal to axis one at index zero. Similarly, the slices $(0, 0)$ and $(1, 1)$ correspond to the left and top boundaries. In three dimensions we have $(0, 0)$, $(0, 1)$, $(1, 0)$, $(1, 1)$, $(2, 0)$, and $(2, 1)$ for the functions with support on the left, right, front, back, bottom, and top faces, respectively.

To keep track of active and inactive shape functions in the tensor-product, we introduce a *tensor-product mask*, a d -dimensional tensor of Boolean values. An entry T_α , with $\alpha = (\alpha_0, \dots, \alpha_{d-1})$ in this tensor-product mask determines whether the shape function N_α is active or not. All shape functions with indices outside the shape of T are implicitly inactive. Therefore, T must be large enough to include all active shape functions. Figure 4a shows the tensor-product mask corresponding to

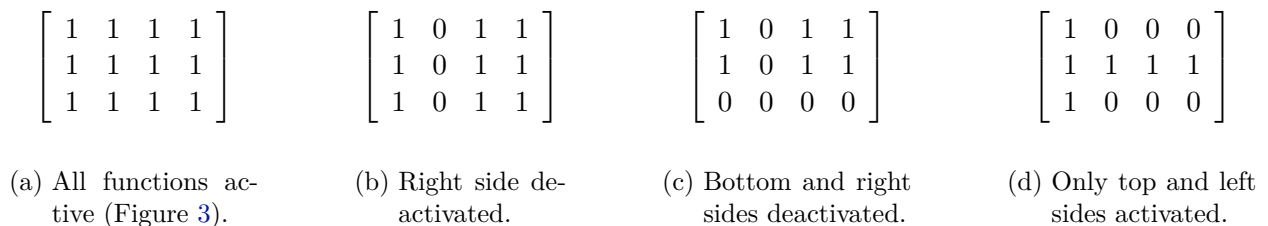


Figure 4. Tensor-product masks in two dimensions.

Figure 3, where all shape functions are active. We then impose homogeneous boundary conditions on the right side (Figure 4b) and then additionally on the bottom side (Figure 4c). Figure 4d shows the result of activating the left and top boundary functions starting from a cell without any active functions.

Remark 3.1 *The hierarchical nature of the basis allows us to use inhomogeneous polynomial degrees between elements. If two connected elements have varying degrees in the tangential direction(s), we cannot combine non-hierarchical shape functions to obtain globally continuous basis functions.*

Remark 3.2 *The integrated Legendre polynomials (2) can be expanded and evaluated using Horner's scheme. However, the recursive definition we use is computationally more efficient when we compute all shape functions $I_0 - I_p$ at once.*

4. Global multi-level hp -basis

We now construct an hp -basis supported on the refinement tree described in Section 2. To this end, we assign each finite element a set of polynomial degrees. To visualize the algorithm, we use the mesh that Figure 1 shows and assign the polynomial degrees (3, 2) to cell 3 and the polynomial degrees (2, 1) to all refined cells.

4.1. Tensor-product masks

In the following, we introduce an algorithm for constructing a *tensor-product mask* for each cell. This mask selects the active shape functions from the full tensor-product space formed by the integrated Legendre shape functions needed to assemble compatible, linearly independent global basis functions. A key operation in this algorithm is to restore compatibility along cell interfaces arising from non-

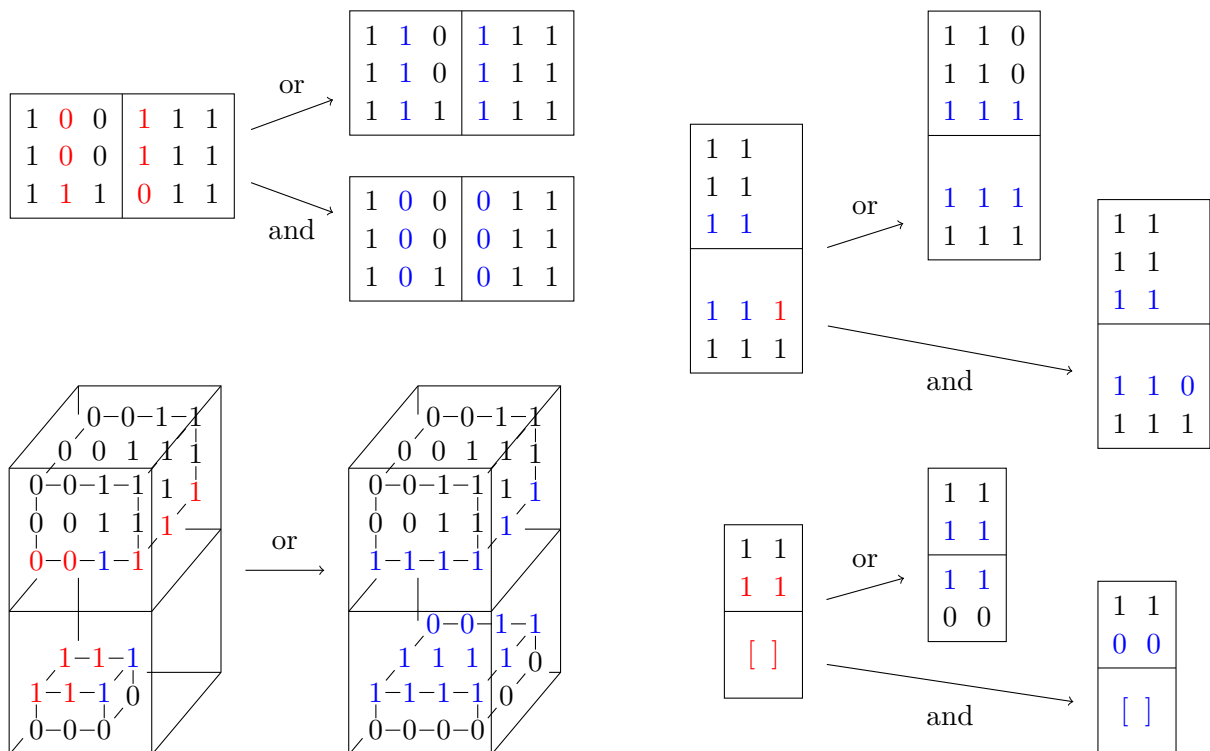


Figure 5. Logical operations on tensor-product masks. Incompatible entries in the corresponding slices are colored red, compatible entries are colored blue.

matching *tensor-product masks*. Suppose the entries in the two corresponding slices are different (e.g., on one side, all shape functions are inactive, on the other side, all shape functions are active);

then, we compare the sets of basis functions using either a logical *and* or a logical *or* and set both slices equal to the result. Figure 5 shows some examples of the two operations. When operating on masks of different sizes using a logical *or* operation, we may need to resize either or both sides. In that case, we initialize new entries to zero, as Figure 5 exemplifies. Now, we define the central algorithm, which guarantees continuity of the overall *hp*-approximation.

1. Assign a tensor-product mask to each cell of the refinement tree. We initialize the leaf-cell masks according to their associated polynomial degrees; all shape functions of non-leaf cells are inactive. Figure 6 shows the initial masks for the refined grid sketched in Figure 1. In this state, the shape functions cannot combine into C^0 , linearly independent global basis functions since the shape functions on the internal boundary of the overlay patch are active. Furthermore, on cell interfaces of the base mesh, we activate all functions for non-refined cells and no functions on cells with overlay cells.

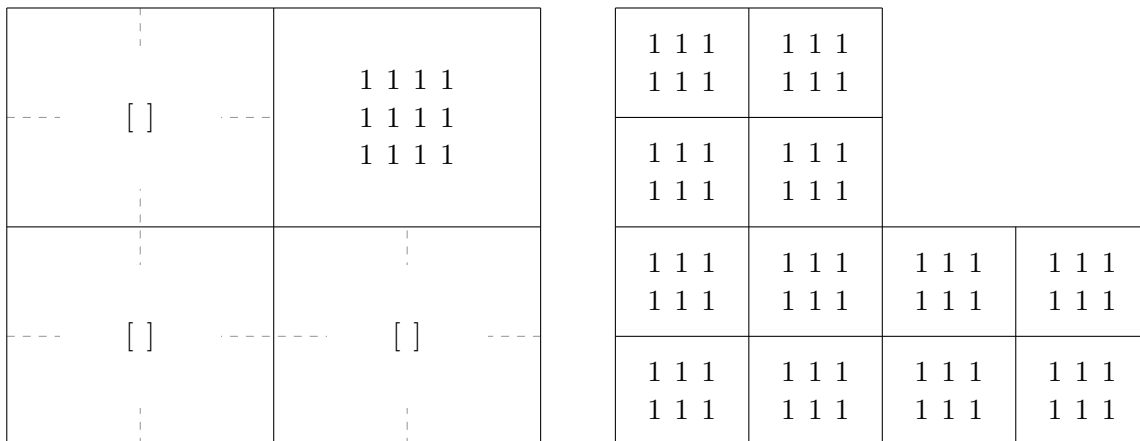


Figure 6. Initialize tensor-product masks (step 1): $p = (3, 2)$ on level 0 and $p = (2, 1)$ on level 1.

2. Restore continuity on cell interfaces. For each cell interface, we consider the two corresponding slices of the tensor-product masks and combine them with a logical *or* operation; then, we overwrite the slices on both sides with the result of this operation. We repeat the process of looping over all cells d times (d iterations). Figure 7 shows two iterations of step 2 for the base mesh; this example does not modify the overlay cells (and hence not shown), but generally, we must consider all cells. The first iteration activates the functions on the right edge of cell 1 (top left) and the top edge of cell 2 (bottom right). If we consider the linear basis function associated with the central node, then the shape function contributing from the bottom left cell is still inactive after the first step. Hence, we repeat the previous step to communicate this update to the neighbors of our cell's

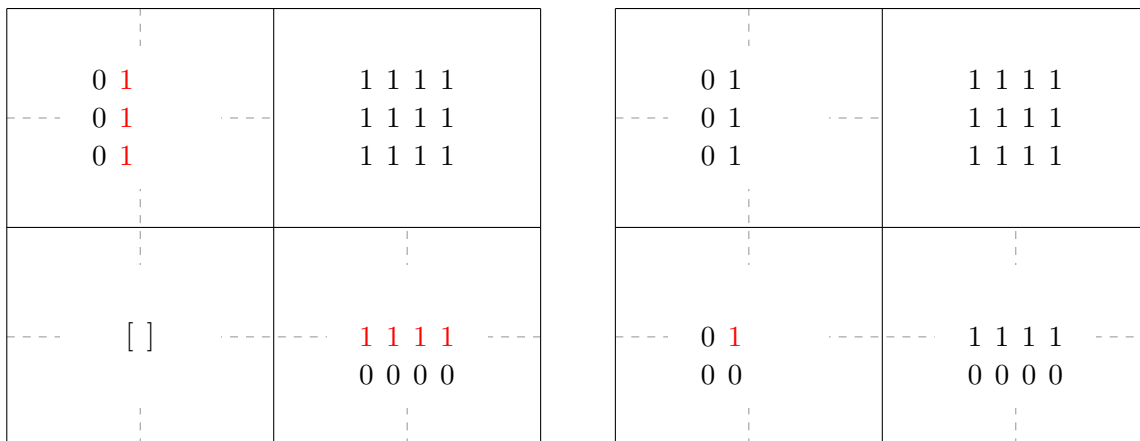


Figure 7. Communicate active functions to neighbors (step 2). Changed entries are colored red.

neighbors. In general, for a grid with a Cartesian topology, each new spatial dimension requires one additional iteration. For example, we need to communicate along three faces in three dimensions to reach all cells connected to a node. Our implementation uses the simplest form of this algorithm, where we communicate over all interfaces in each iteration. Additionally, this step restores continuity for inhomogeneous polynomial distributions between cells (for each shared spatial dimension). If two adjacent cells do not share the same polynomial degree(s) in the interface direction(s), this step activates shape functions on the boundary of cells when they are active in the neighboring cells.

3. Deactivate shape functions on internal boundaries. If a cell has a neighbor of different refinement level on a side, then we deactivate the slice in its tensor-product corresponding to that side, as Figure 8 shows.

1 1 1	1 0 1		
1 1 1	1 0 1		
1 1 1	1 0 1		
1 1 1	1 0 1		
1 1 1	1 1 1	0 0 0	0 0 0
1 1 1	1 1 1	1 1 1	1 1 1
1 1 1	1 1 1	1 1 1	1 1 1
1 1 1	1 1 1	1 1 1	1 1 1

Figure 8. Deactivate internal boundaries (step 3).

1 1 1	1 0 1		
1 1 1	1 0 1		
1 1 1	1 0 1		
1 1 1	1 0 1		
1 1 1	1 0 1	0 0 0	0 0 0
1 1 1	1 1 1	1 1 1	1 1 1
1 1 1	1 1 1	1 1 1	1 1 1
1 1 1	1 1 1	1 1 1	1 1 1

Figure 9. Communicate zero Dirichlet conditions to neighbors (step 4).

4. Communicate deactivated functions along cell interfaces. Repeat the process step 2 using the logical *and* operation instead. This communicates the changes from step 3 to the neighbors; it is sufficient to perform only $d - 1$ iterations in step 4, see Figure 9.

At this point, we obtain the correct tensor-product masks for all finite elements, which allows us to evaluate the basis functions in each finite element. We first evaluate the integrated Legendre polynomials in each direction and then compute the active entries within the tensor-product according to the corresponding mask. If needed, we map the derivatives into the global coordinate system (physical space). We start on a leaf cell and repeat this process for each parent cell in the hierarchy towards the root cell. With each new level, we map the evaluation coordinates accordingly.

Remark 4.1

The hierarchical nature of the integrated Legendre shape functions allows to remove certain modes from the tensor-product that do not contribute to order of convergence. The result is commonly referred to as the trunk space. Appendix A derives the corresponding initial tensor-product masks applied in step 1 of the algorithm introduced here.

Remark 4.2

We introduce the tensor-product masks as individual tensors. Alternatively, one could first determine bounds for their size and then allocate them once potentially in a contiguous fashion.

4.2. Location maps

In our second algorithm, we use the topological data of Section 2 to construct location maps that connect the local element shape functions from the previous section to globally compatible *hp* basis functions, which is done as follows.

1. **Assign a unique global identifier (id) to each active local shape function.** Currently, the shape functions of different cells are not connected. Figure 10 shows the initial global indices corresponding to the tensor-product masks of the present example (cf. Figures 7 and 9).

-1	3	10	13	16	19
-1	2	9	12	15	18
-1	1	8	11	14	17
-1	0	4	5	6	7
-1	-1	-1	-1	-1	-1

50	52	54	60	-1	62						
49	51	53	59	-1	61						
44	46	48	56	-1	58						
43	45	47	55	-1	57						
27	29	31	39	-1	42	-1	-1	-1	-1	-1	-1
26	28	30	38	40	41	69	70	71	78	79	80
21	23	25	33	35	37	64	66	68	73	75	77
20	22	24	32	34	36	63	65	67	72	74	76

Figure 10. Assign each active local shape function a unique global index.

2. **Connect shape functions along cell interfaces.** We loop over all coordinate axes and identify the normal cell interfaces. For each interface we set the indices on one side equal to the indices on the other. Figure 11 shows this process first along interfaces normal to x , then along interfaces normal to y . This step leaves gaps in the global numbering.

-1	3	3	13	16	19
-1	2	2	12	15	18
-1	1	1	11	14	17
-1	0	0	5	6	7
-1	-1	-1	-1	-1	-1

50	52	54	52	-1	62						
49	51	53	51	-1	61						
44	46	48	46	-1	58						
43	45	47	45	-1	57						
27	29	31	29	-1	42	-1	-1	-1	-1	-1	-1
26	28	30	28	40	41	40	70	71	70	79	80
21	23	25	23	35	37	35	66	68	66	75	77
20	22	24	22	34	36	34	65	67	65	74	76

-1	3	3	13	16	19
-1	2	2	12	15	18
-1	0	0	5	6	7
-1	0	0	5	6	7
-1	-1	-1	-1	-1	-1

50	52	54	52	-1	62						
44	46	48	46	-1	58						
44	46	48	46	-1	58						
27	29	31	29	-1	42						
27	29	31	29	-1	42	-1	-1	-1	-1	-1	-1
21	23	25	23	35	37	35	66	68	66	75	77
21	23	25	23	35	37	35	66	68	66	75	77
20	22	24	22	34	36	34	65	67	65	74	76

Figure 11. Combine adjacent shape functions to global basis functions (join first in x , then in y).

3. Eliminate gaps in the global numbering. We determine which indices still have contributions and assign a reduced set of indices to them. In Figure 12, we create an index map and show the result after applying this map to the indices from the previous step.

```

old index: 0 1 2 3 4 5 6 7 8 9 10 11 12 13 14 15 16 17 18 19 20 21 22 23 24 25 26
exists:    1 0 1 1 0 1 1 1 0 0 0 0 1 1 0 1 1 0 1 1 1 1 1 1 1 1 0
new index: 0 -1 1 2 -1 3 4 5 -1 -1 -1 -1 6 7 -1 8 9 -1 10 11 12 13 14 15 16 17 -1

old index: 27 28 29 30 31 32 33 34 35 36 37 38 39 40 41 42 43 44 45 46 47 48 49 50 51 52 53
exists:    1 0 1 0 1 0 0 1 1 1 1 0 0 0 0 1 0 1 0 1 0 1 0 1 0 1 0
new index: 18 -1 19 -1 20 -1 -1 21 22 23 24 -1 -1 -1 -1 25 -1 26 -1 27 -1 28 -1 29 -1 30 -1

old index: 54 55 56 57 58 59 60 61 62 63 64 65 66 67 68 69 70 71 72 73 74 75 76 77 78 79 80
exists:    1 0 0 0 1 0 0 0 1 0 0 1 1 1 1 0 0 0 0 0 1 1 1 1 0 0 0
new index: 31 -1 -1 -1 32 -1 -1 -1 33 -1 -1 34 35 36 37 38 -1 -1 -1 -1 39 40 41 42 -1 -1 -1

```

<table style="width: 100%; border-collapse: collapse;"> <tr> <td style="border: none; width: 50%; padding: 5px;"> <table style="width: 100%; border-collapse: collapse;"> <tr><td style="border: none; width: 50%; padding: 5px;">-1 2</td><td style="border: none; width: 50%; padding: 5px;">2 7 9 11</td></tr> <tr><td style="border: none; padding: 5px;">-1 1</td><td style="border: none; padding: 5px;">1 6 8 10</td></tr> <tr><td style="border: none; padding: 5px;">-1 0</td><td style="border: none; padding: 5px;">0 3 4 5</td></tr> </table> </td> <td style="border: none; padding: 5px;"> </td> </tr> <tr> <td style="border: none; padding: 5px;">-1 0</td> <td style="border: none; padding: 5px;">0 3 4 5</td> </tr> <tr> <td style="border: none; padding: 5px;">-1 -1</td> <td style="border: none; padding: 5px;">-1 -1 -1 -1</td> </tr> </table>	<table style="width: 100%; border-collapse: collapse;"> <tr><td style="border: none; width: 50%; padding: 5px;">-1 2</td><td style="border: none; width: 50%; padding: 5px;">2 7 9 11</td></tr> <tr><td style="border: none; padding: 5px;">-1 1</td><td style="border: none; padding: 5px;">1 6 8 10</td></tr> <tr><td style="border: none; padding: 5px;">-1 0</td><td style="border: none; padding: 5px;">0 3 4 5</td></tr> </table>	-1 2	2 7 9 11	-1 1	1 6 8 10	-1 0	0 3 4 5		-1 0	0 3 4 5	-1 -1	-1 -1 -1 -1	<table style="width: 100%; border-collapse: collapse;"> <tr> <td style="border: none; width: 50%; padding: 5px;">29 30 31</td> <td style="border: none; width: 50%; padding: 5px;">30 -1 33</td> <td style="border: none;"> </td> <td style="border: none;"> </td> </tr> <tr> <td style="border: none; padding: 5px;">26 27 28</td> <td style="border: none; padding: 5px;">27 -1 32</td> <td style="border: none;"> </td> <td style="border: none;"> </td> </tr> <tr> <td style="border: none; padding: 5px;">26 27 28</td> <td style="border: none; padding: 5px;">27 -1 32</td> <td style="border: none;"> </td> <td style="border: none;"> </td> </tr> <tr> <td style="border: none; padding: 5px;">18 19 20</td> <td style="border: none; padding: 5px;">19 -1 25</td> <td style="border: none;"> </td> <td style="border: none;"> </td> </tr> <tr> <td style="border: none; padding: 5px;">18 19 20</td> <td style="border: none; padding: 5px;">19 -1 25</td> <td style="border: none; padding: 5px;">-1 -1 -1</td> <td style="border: none; padding: 5px;">-1 -1 -1</td> </tr> <tr> <td style="border: none; padding: 5px;">13 15 17</td> <td style="border: none; padding: 5px;">15 22 24</td> <td style="border: none; padding: 5px;">22 35 37</td> <td style="border: none; padding: 5px;">35 40 42</td> </tr> <tr> <td style="border: none; padding: 5px;">13 15 17</td> <td style="border: none; padding: 5px;">15 22 24</td> <td style="border: none; padding: 5px;">22 35 37</td> <td style="border: none; padding: 5px;">35 40 42</td> </tr> <tr> <td style="border: none; padding: 5px;">12 14 16</td> <td style="border: none; padding: 5px;">14 21 23</td> <td style="border: none; padding: 5px;">21 34 36</td> <td style="border: none; padding: 5px;">34 39 41</td> </tr> </table>	29 30 31	30 -1 33			26 27 28	27 -1 32			26 27 28	27 -1 32			18 19 20	19 -1 25			18 19 20	19 -1 25	-1 -1 -1	-1 -1 -1	13 15 17	15 22 24	22 35 37	35 40 42	13 15 17	15 22 24	22 35 37	35 40 42	12 14 16	14 21 23	21 34 36	34 39 41
<table style="width: 100%; border-collapse: collapse;"> <tr><td style="border: none; width: 50%; padding: 5px;">-1 2</td><td style="border: none; width: 50%; padding: 5px;">2 7 9 11</td></tr> <tr><td style="border: none; padding: 5px;">-1 1</td><td style="border: none; padding: 5px;">1 6 8 10</td></tr> <tr><td style="border: none; padding: 5px;">-1 0</td><td style="border: none; padding: 5px;">0 3 4 5</td></tr> </table>	-1 2	2 7 9 11	-1 1	1 6 8 10	-1 0	0 3 4 5																																							
-1 2	2 7 9 11																																												
-1 1	1 6 8 10																																												
-1 0	0 3 4 5																																												
-1 0	0 3 4 5																																												
-1 -1	-1 -1 -1 -1																																												
29 30 31	30 -1 33																																												
26 27 28	27 -1 32																																												
26 27 28	27 -1 32																																												
18 19 20	19 -1 25																																												
18 19 20	19 -1 25	-1 -1 -1	-1 -1 -1																																										
13 15 17	15 22 24	22 35 37	35 40 42																																										
13 15 17	15 22 24	22 35 37	35 40 42																																										
12 14 16	14 21 23	21 34 36	34 39 41																																										

Figure 12. Elimination of unassigned global basis function indices.

4. Linearize indices and append parent indices. To obtain the location maps for our finite elements (leaf cells), we linearize the indices obtained in step 3 and append all parent levels. Figure 13 shows the resulting location maps.

element 0 : [0, 1, 2, 3, 6, 7, 4, 8, 9, 5, 10, 11]	element 7 : [19, 27, 25, 32, 0, 1, 2]
element 1 : [12, 13, 14, 15, 16, 17, 0]	element 8 : [27, 30, 32, 33, 0, 1, 2]
element 2 : [13, 18, 15, 19, 17, 20, 0]	element 9 : [21, 22, 34, 35, 36, 37, 0, 3, 4, 5]
element 3 : [14, 15, 21, 22, 23, 24, 0]	element 10 : [22, 35, 37, 0, 3, 4, 5]
element 4 : [15, 19, 22, 24, 25, 0]	element 11 : [34, 35, 39, 40, 41, 42, 0, 3, 4, 5]
element 5 : [18, 26, 19, 27, 20, 28, 0, 1, 2]	element 12 : [35, 40, 42, 0, 3, 4, 5]
element 6 : [26, 29, 27, 30, 28, 31, 0, 1, 2]	

Figure 13. Final location maps after appending base cell location maps (colored accordingly).

Now, we have all information needed to assemble a global finite element matrix system, for example.

Remark 4.3

The chosen example features only one level of refinement. The algorithms, however, apply to arbitrary nested space-tree partitions. We only distinguish between leaf- and non-leaf cells and between different types of cell boundaries.

Remark 4.4

In practice, one might encapsulate the topological and geometric data from Section 2 into a mesh data type and encapsulate the results of this section into an hp-basis data type.

Remark 4.5

Instead of storing concatenated location maps for each leaf as suggested in step 4 it may be beneficial to keep the location maps for all cells and append parent indices on-the-fly.

5. Numerical examples

In this section, we use our hierarchical framework to build several adaptive meshes. We implement the algorithms and data structures described in C++ in a dimensionally independent manner. To avoid dynamic memory allocations and enable aggressive compiler optimizations, we define a list of dimensions to instantiate at compile time. The source code for all examples is available at <https://gitlab.com/phmkopp/nd-mlhp-examples>.

5.1. Corner singularity

The first example uses the following manufactured solution

$$u = \sqrt{r} \quad \text{with} \quad r = \sqrt{\sum_{i=0}^{d-1} x_i^2} \quad (5)$$

on $\Omega = [0, 1]^d$ with $d \geq 2$ that features a singularity at $x = 0$. Substituting (5) into (1) and using $\kappa = 1$ yields

$$f = \frac{3 - 2d}{4} r^{-3/2}.$$

We impose homogeneous Neumann boundary conditions on the sides intersecting the coordinate planes: the left and bottom edges in two dimensions, and the left, bottom, and front faces in three dimensions. On the remaining faces, we impose Dirichlet boundary conditions.

We discretize the domain $\Omega = [0, 1]^d$ using a base mesh with two elements in each direction. We perform two refinement studies where each new computation adds another refinement level towards the singularity at the origin. The first strategy uses a full tensor-product space with a uniform polynomial degree p equal to $r + 1$, where r is the maximum refinement level. The second strategy employs a trunk space with a linear grading from $p = r + 1$ on the base elements to $p = 1$ on the elements with refinement level r . Figure 14 shows the graded polynomial degree distribution with one until four levels of refinement and the numerical solution using a uniform tensor-product space with $p = 5$ and $r = 4$. Figure 15 shows the convergence results for different spatial dimensions.

While the convergence of the discretization error versus the number of unknowns is necessary to gain insight into the method's approximation quality, we ultimately believe the method's success depends almost exclusively on runtime performance and memory consumption. We now show that we achieve exponential convergence in terms of these crucial quantities. We use a diagonally pre-conditioned conjugate gradient method to solve the finite element system. Therefore, the number of non-zeros in the matrix dominates the memory consumption. The two most significant contributions to the runtime are the assembly and the solution of the linear system.

In the following, we analyze the asymptotic behavior of these quantities on the example. To allow comparisons with runtime measurements, we perform our analysis in terms of the refinement study index r . For brevity, we focus on the full tensor-product space using a uniform polynomial degree

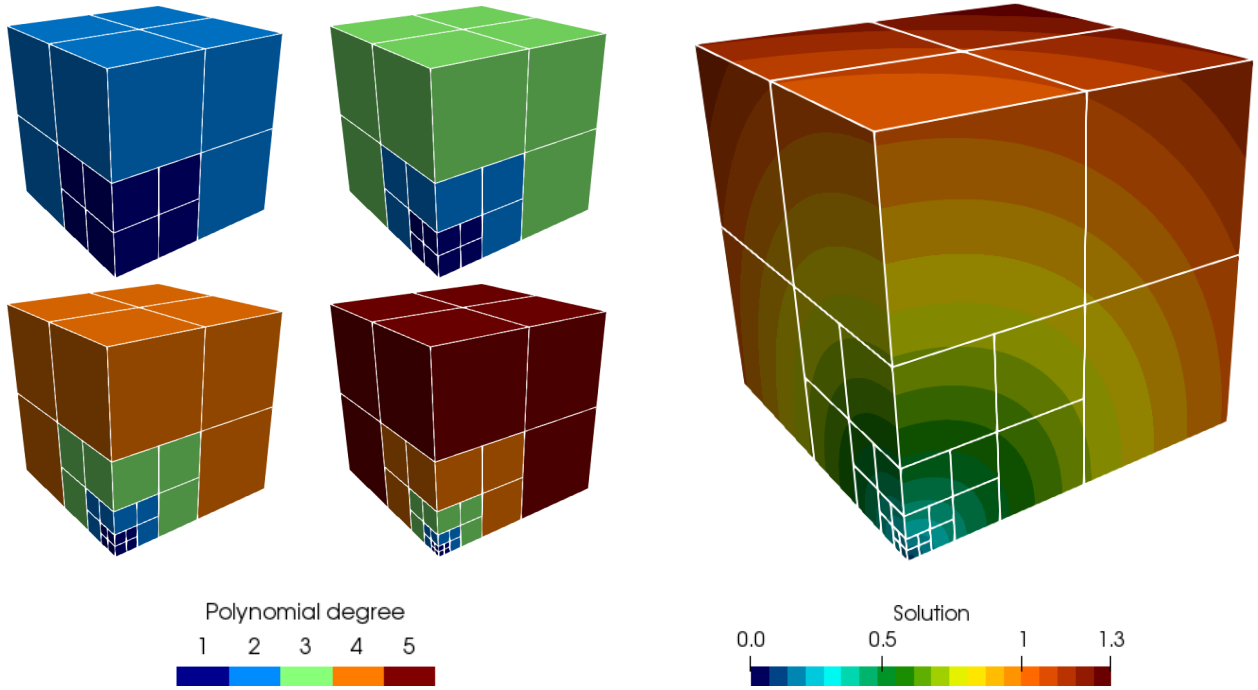


Figure 14. Graded polynomial degree distribution for $r = 1 - 4$ (left) and solution for $r = 4$ (right).

elevation. Each new refinement level adds 2^d cells that overlay the cell in the origin of the parent level. We can therefore compute the number of elements (leaf cells) as $r(2^d - 1) + 1 = \mathcal{O}(r)$.

Each leaf cell contributes to at most $(p + 1)^d \sim p^d$ basis functions defined on the same refinement level, but it also receives contributions from all coarser levels. The key to why we get good scaling is that parent cells only contribute basis functions active on their boundary. This results in at most $(p + 1)^d - (p - 1)^d \sim p^{d-1}$ functions per (coarser) level. Because $r \sim p$, we can conclude that these contributions scale with

$$\mathcal{O}(rp^{d-1}) \xrightarrow{r \sim p} \mathcal{O}(p^d)$$

and hence are of the same order as the $(p - 1)^d = \mathcal{O}(p^d)$ internal functions coming from the classical p -version of the finite element method.

We then bound the number of non-zeros in the assembled matrix to some value between the sum of all element matrix sizes (upper bound) and the sum of all internal contributions (lower bound). Using $\mathcal{O}(rp^{d-1} + p^d)$ as upper-bound for the number of element unknowns and multiplying with $\mathcal{O}(r)$ number of elements yields

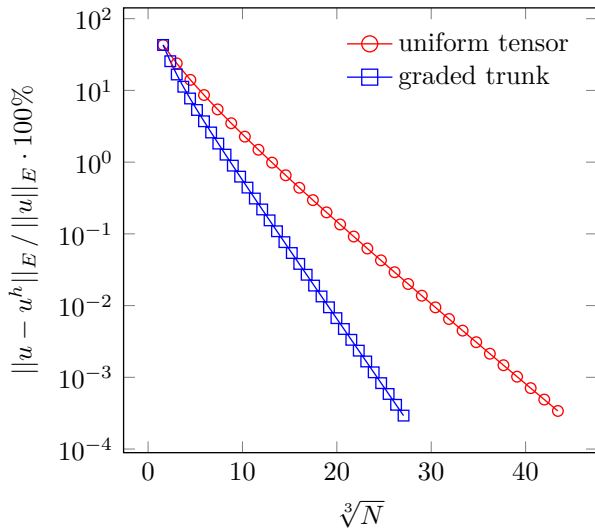
$$\mathcal{O}(r) \mathcal{O}(rp^{d-1} + p^d)^2 \xrightarrow{r \sim p} \mathcal{O}(p^{2d+1})$$

as an estimate of the complexity for the number of non-zeros in the assembled sparse matrix. The same result is obtained when considering only internal contributions.

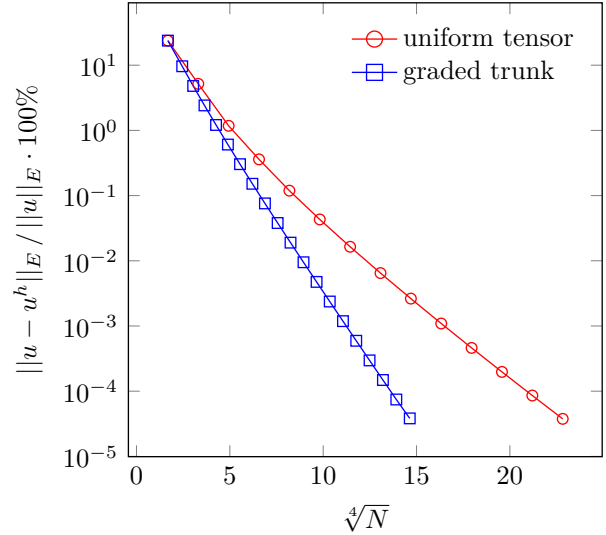
Similarly, we estimate the assembly effort by summing up the number of operations needed to integrate each element matrix numerically. Assuming a standard Gauss-Legendre quadrature, we need $(p + 1)^d = \mathcal{O}(p^d)$ integration points, on which we evaluate an outer product of $\mathcal{O}(rp^{d-1} + p^d)$ shape functions. Together, we obtain

$$\mathcal{O}(r) \mathcal{O}(p^d) \mathcal{O}(rp^{d-1} + p^d)^2 \xrightarrow{r \sim p} \mathcal{O}(p^{3d+1}).$$

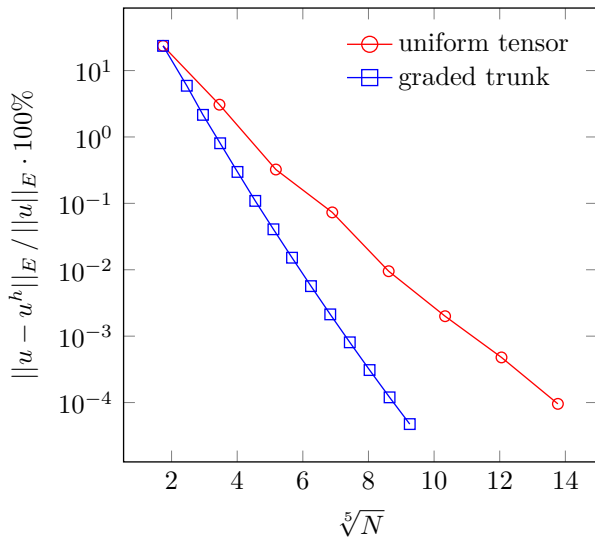
Figure 16 shows that the number of non-zeros scales as the analysis above shows, while that the number of conjugate gradient iterations increases roughly with p^{d-1} ; the analysis of this empirical observation depends on the condition number of the sparse matrix that exceeds the scope of this work. We iterate until $\sqrt{r \cdot D(r)} < 10^{-10}$, where $D(r)$ is the diagonal preconditioner applied to the residual $r = Ax - b$. Moreover, we are not utilizing the symmetry of the sparse matrix, which significantly



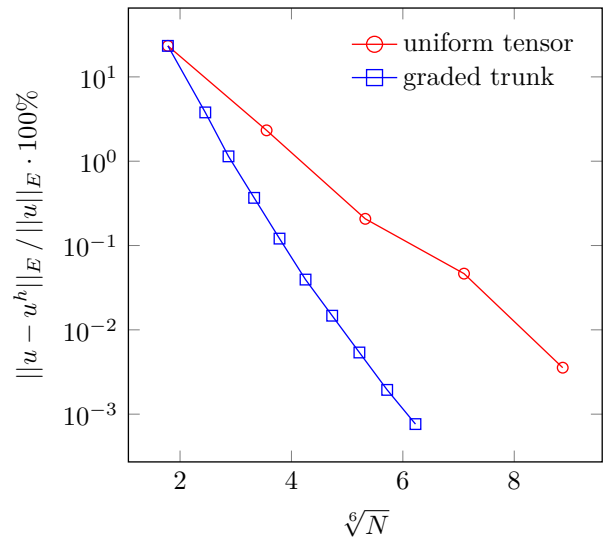
(a) 2D



(b) 3D



(c) 4D



(d) 5D

Figure 15. Convergence of the error in the energy norm.

simplifies the parallel implementation of the sparse matrix-vector product. By combining the results for the number of non-zeros with the number of iterations, we estimate the runtime complexity for our iterative solver as $\mathcal{O}(p^{3d})$. Although the theoretical scaling of the assembly of the linear system is an \mathcal{O} of higher order, it did not dominate the total runtime on this example, as Figure 16 shows. Also, for the type of meshes used in this example, it is even possible to construct direct solvers with a linear complexity with respect to the number of unknowns [14].

The measurements change significantly when considering the trunk space with the graded polynomial degree distribution. While the overall scaling is the same, the absolute effort per degree of freedom is higher, and the relative runtime of the assembly increases compared to the linear solution. We identify three aspects that are responsible for these differences. First, although the fine levels were assigned a lower polynomial degree, they still obtain contributions from the higher-order base elements. Due to these, even the finest level with $p = 1$ requires $r + 2$ Gauss-Legendre points per direction to integrate the parent contributions sufficiently accurate. Second, removing internal modes increases the connectivity in the trunk space, resulting in higher runtime and increased memory consumption per unknown. And third, if we consider two interacting shape functions N_i and N_j ,

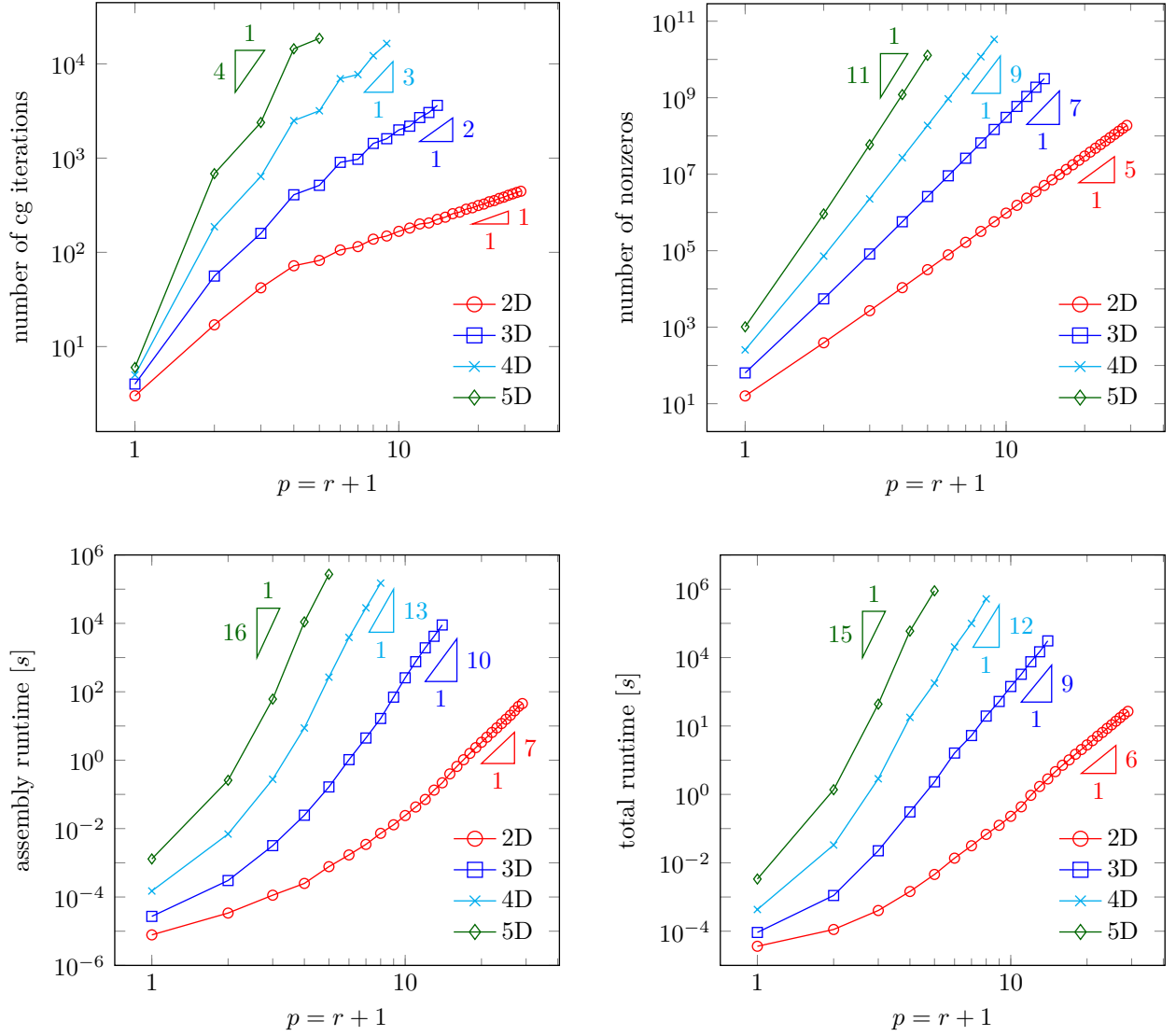


Figure 16. Number of conjugate gradient iterations, number of non-zeros in the sparse matrix and serial runtime comparison. The total runtime excludes the error computation.

then the effort for assembling this interaction is proportional to the number of elements N_i and N_j overlap. Internal functions overlap only on one element, but functions active on boundaries overlap at least two elements, making internal functions cheaper to assemble. After the assembly, however, this interaction results in a single entry in the sparse matrix regardless of the number of elements the supports overlap.

5.2. Transient problem with dynamic (de-)refinement

We demonstrate the effectiveness of the dynamic refinement and derefinement considering the transient version of (1) with constant coefficients c and κ :

$$\begin{aligned}
 c\dot{u} - \kappa\Delta u &= f && \text{on } \Omega \times T \\
 u &= u_0 && \text{at } t = 0 \\
 u &= u_b && \text{on } \Gamma_D \\
 n \cdot \kappa\nabla u &= 0 && \text{on } \Gamma_N.
 \end{aligned} \tag{6}$$

We discretize (6) using method of Rothe, which discretizes time first and therefore allows for non-matching spatial discretizations in each time-step (as opposed to the method of lines, which discretizes

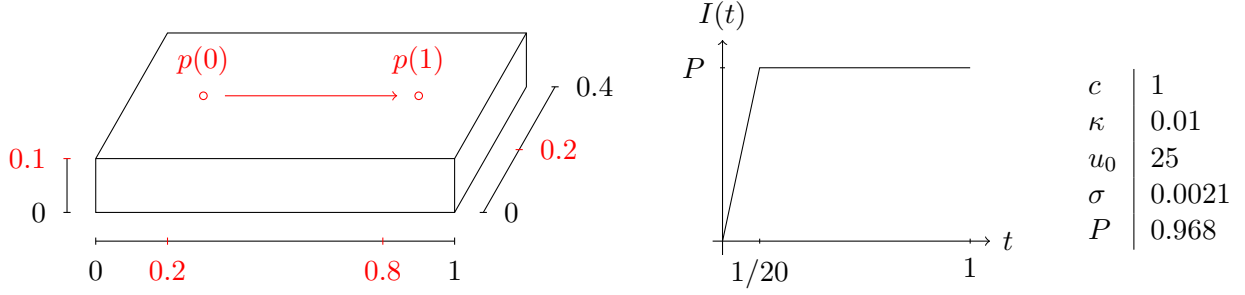


Figure 17. Domain and path definitions, intensity function and problem parameters.

space first). We rewrite the domain part of (6) as $c\dot{u} = f + \kappa\Delta u$ and apply the general- θ method:

$$\frac{c}{\Delta t} (u^{n+1} - u^n) = \theta (f^{n+1} + \kappa\Delta u^{n+1}) + (1 - \theta) (f^n + \kappa\Delta u^n), \quad (7)$$

where $\theta = 0$ and $\theta = 1$ yield the first-order explicit and implicit Euler methods and $\theta = 1/2$ yields the second-order implicit midpoint (Crank-Nicolson) rule. Reorganizing the terms in (7) yields

$$\frac{c}{\Delta t} u^{n+1} - \kappa\theta\Delta u^{n+1} = \frac{c}{\Delta t} u^n + \kappa(1 - \theta)\Delta u^n + \theta f^{n+1} + (1 - \theta)f^n. \quad (8)$$

We then discretize the weak form of (8) to obtain a system of equations $K_{ij}^{n+1} \hat{u}_j^{n+1} = F_i^{n+1}$, where

$$\begin{aligned} K_{ij}^{n+1} &= \int_{\Omega} \frac{c}{\Delta t} N_i N_j + \kappa\theta \nabla N_i \cdot \nabla N_j \, d\Omega \\ F_i^{n+1} &= \int_{\Omega} N_i \left(\frac{c}{\Delta t} u^n + \theta f^{n+1} + (1 - \theta)f^n \right) - \kappa(1 - \theta) \nabla N_i \cdot \nabla u^n \, d\Omega. \end{aligned} \quad (9)$$

The basis functions N_i and N_j in (9) belong to the time-slice t^{n+1} . The old solution u^n and its derivatives ∇u^n , however, belong to the time-slice t^n . The representation of the solution in two time-slices requires our implementation to provide two bases (for t^n and for t^{n+1}) to assemble the equation system resulting from one time-step. Furthermore, we ensure C^∞ continuity on each integration cell by distributing Gauss-Legendre points on the intersection of both grids.

Now, we demonstrate the performance and consistency of the two-time-slice representation on an example motivated by the simulation of powder bed fusion processes in additive manufacturing, where a laser selectively melts the metal powder in a layer-by-layer fashion. We choose a volumetric heat source in the shape of a Gaussian bell function that travels along a path $p(t)$ with varying intensity $I(t)$. We therefore have

$$f(x, t) = I(t) q(x - p(t)),$$

with

$$q(x) = \frac{1}{(2\pi)^{d/2} \sigma^d} \exp\left(\frac{-x_i^2}{2\sigma^2}\right).$$

Assuming that $I(t) = 0$ for $t < 0$ and $u(x, 0) = u_0 = \text{const}$, we obtain the following semi-analytical solution on an infinite domain:

$$\begin{aligned} u(x, t) &= \int_0^t I(\tau) g(x - p(\tau), t - \tau) \, d\tau + u_0 \\ g(x, t) &= \frac{1}{c(2\pi)^{d/2} w(t)^d} \exp\left(\frac{-x_i^2}{2w(t)^2}\right) \\ w(t) &= \sqrt{\sigma^2 + \frac{2\kappa t}{c}}. \end{aligned} \quad (10)$$

Here, g represents the solution to (6) with $f = q(x)\delta(t)$. We then restrict Ω and T to a three-dimensional cube on the time interval $[0, 1]$ and select a linear source path on the top face. Figure 17 shows the geometric setup and the physical parameters we use. To conform to (10), we choose homogeneous boundary conditions on the top face due to symmetry and Dirichlet boundary conditions on all other faces.

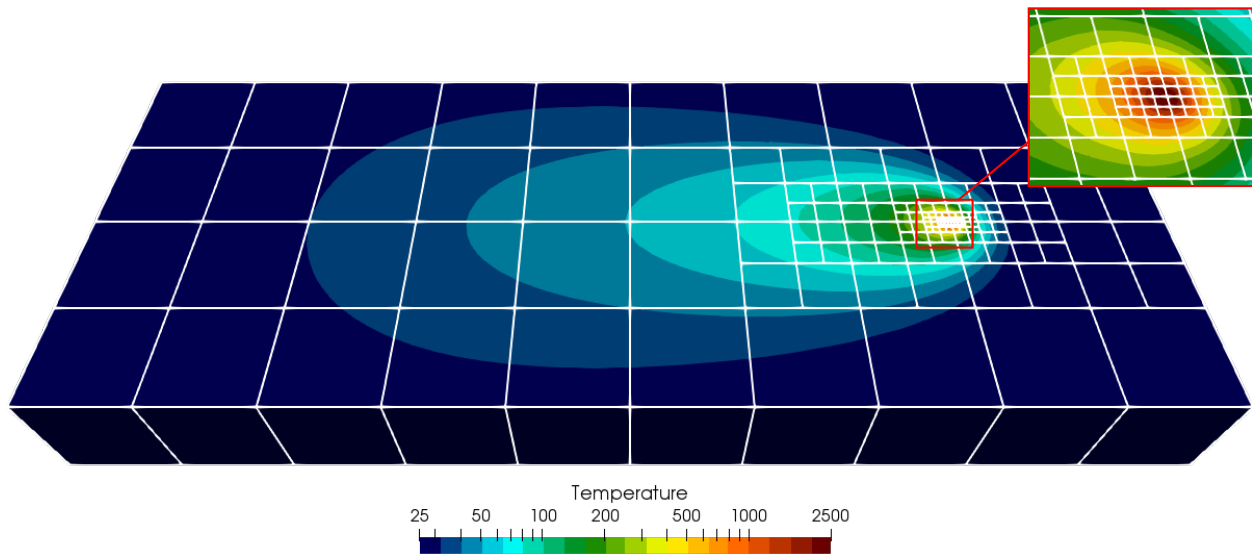
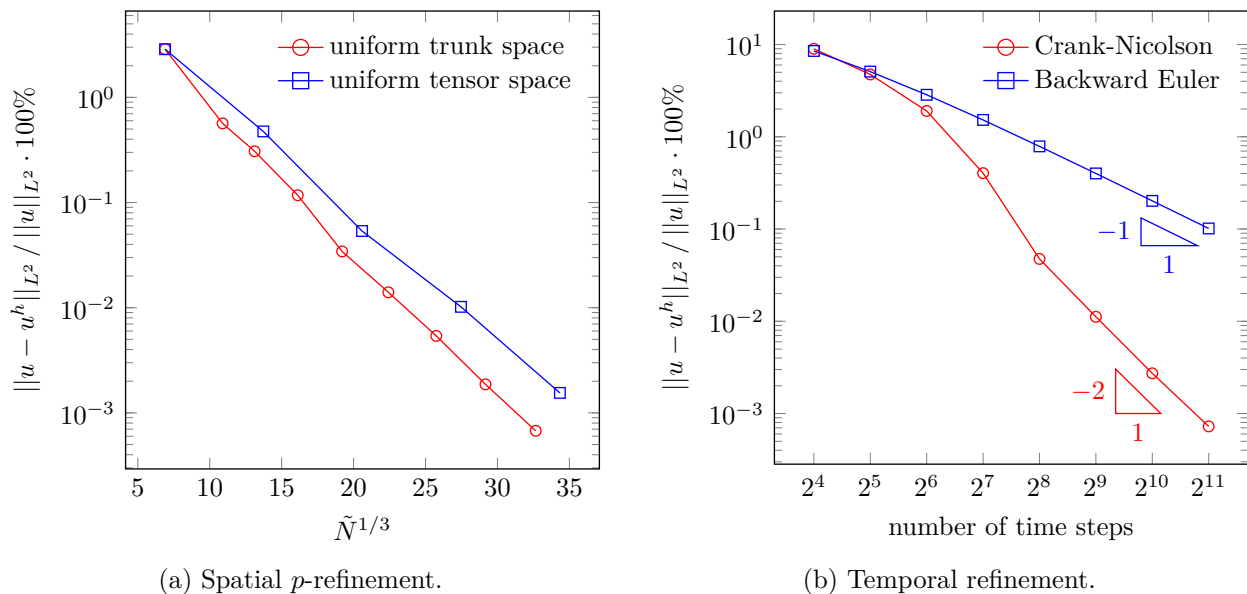


Figure 18. Solution at $t = 1$ using a logarithmic color map.

Figure 18 shows the solution at $t = 1$ after 256 Crank-Nicolson steps using a dynamic local refinement. We set the polynomial degrees to 5, 5, 4, 3, 3 and 2 for refinement levels 0 to 5, respectively, resulting in an average of 4190 unknowns per time-step. The computation was performed on a Desktop computer using an i9-9900KF processor with all eight cores running at 4.6 GHz. The complete simulation took 189.9s single-threaded and 28.3s using eight threads. The resulting speedup of 6.7x is remarkable, considering that one time-step takes only about 110ms to compute. The memory required for storing the sparse matrix averaged around 7.2 MB, while the topological information and the basis data together used around 80 kB of memory. We used the g++-10 compiler and 32-bit unsigned integers for cell indices and sparse (= degree of freedom) indices.



(a) Spatial p -refinement.

(b) Temporal refinement.

Figure 19. Convergence of spatial and temporal discretizations.

We then perform convergence studies for spatial and temporal discretizations in terms of the error

in the L^2 norm. In Figure 19a, we increase the polynomial degree for a fixed temporal discretization of 4096 Crank-Nicolson steps. \tilde{N} denotes the average number of unknowns per time-step. Figure 19b shows the convergence of different time marching schemes for a fixed spatial discretization using a trunk space with $p = 10$. For all cases, we use the same locally refined meshes. We evaluate the norms numerically using a trapezoidal rule in time and a Gauss-Legendre quadrature in space with $p + 1$ points per direction on each integration cell. The integral in the semi-analytical solution is again evaluated numerically on each integration point in a stepwise fashion with $dt \approx 1/100$ and 30 Gauss-Legendre points per interval.

6. Conclusion

We describe a data-oriented construction for multi-level hp -bases. The algorithmic framework only operates on the $d - 1$ dimensional slices of the element data, which significantly simplifies the implementation of the method for higher dimensions. While we focus on Cartesian grids here, these data structures and algorithms easily generalize to unstructured meshes. We consider a Fichera corner example to show that our implementation scales well, even for small problem sizes. However, the exponential complexity in the number of spatial dimensions makes high-dimensional computations very expensive regarding runtime and memory consumption. Finally, we apply our methodology to a transient heat equation and show the potential of dynamic local refinement and derefinement in bridging the vastly different spatial scales arising, for example, in powder bed fusion processes. Our next step will be to address spatial and temporal scales using the presented method combined with space-time finite element methods.

A. Construction of initial tensor-product masks for the trunk space

Section 4 mentions that using all functions from the tensor-product is not always necessary. If we consider a monomial basis

$$\left\{ r_0^{\alpha_0} \cdot \dots \cdot r_{d-1}^{\alpha_{d-1}} \mid \text{for } \alpha_i = 0, \dots, p_i \right\}, \quad (11)$$

then picking only functions where $\sum \alpha_i \leq \max p_i$ will not reduce the convergence order. Figure 20 shows the monomials for a tensor-product space with $p = (3, 4)$ compared to the reduced basis containing only polynomials with a combined order smaller or equal to $\max p_i = 4$.

r_1^4	$r_0 r_1^4$	$r_0^2 r_1^4$	$r_0^3 r_1^4$	r_1^4			
r_1^3	$r_0 r_1^3$	$r_0^2 r_1^3$	$r_0^3 r_1^3$	r_1^3	$r_0 r_1^3$		
r_1^2	$r_0 r_1^2$	$r_0^2 r_1^2$	$r_0^3 r_1^2$	r_1^2	$r_0 r_1^2$	$r_0^2 r_1^2$	
r_1	$r_0 r_1$	$r_0^2 r_1$	$r_0^3 r_1$	r_1	$r_0 r_1$	$r_0^2 r_1$	$r_0^3 r_1$
1	r_0	r_0^2	r_0^3	1	r_0	r_0^2	r_0^3
tensor product space				monomial trunk space			

Figure 20. Monomials for $p = (3, 4)$.

As monomials are not suitable for constructing compatible finite element bases, we transfer this concept to integrated Legendre functions. In Section 4, we started our algorithm with a full tensor-product mask for leaf cells. To construct initial trunk space masks, we only activate entries of T_α if $\sum \alpha_i \leq \max p_i$. The integrated Legendre functions are hierarchical except in the first two functions (I_0 and I_1 are linear). As a result, we need to ensure that in no case a function with component $I_0(r_i)$ is active, while the corresponding function with component $I_1(r_i)$ is inactive. Therefore, we take the first slice for each coordinate axis and copy its entries to the second slice. Figures 21 and 22 demonstrate this procedure on two- and three-dimensional examples.

While using a trunk space does not reduce the order of convergence, it can significantly reduce the accuracy for a given setup. When increasing the polynomial degree to compensate, one generally

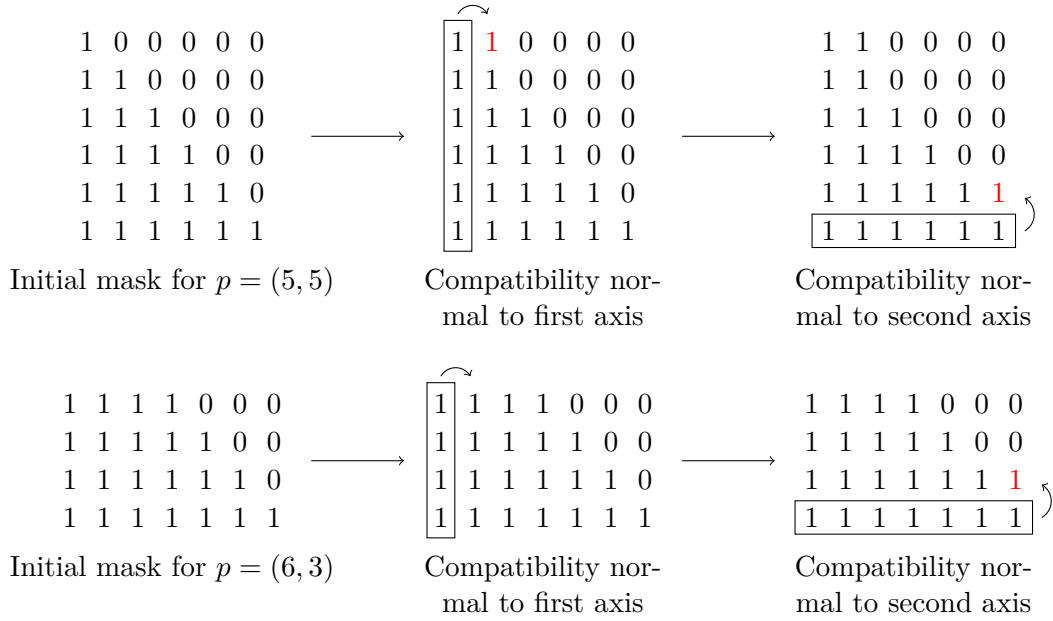


Figure 21. Construction of two-dimensional trunk space initial tensor-product masks.

obtains fewer degrees of freedom for a given accuracy, at the cost of having higher connectivity per unknown. With higher dimensions, the difference between both becomes more pronounced as the limit for $p \rightarrow \infty$ yields $d!$ times fewer unknowns per element (assuming uniform p in all directions). This limit derives from considering an n -simplex in d dimensional space with one vertex at the origin and one vertex on each coordinate axis with distance 1. The volume of this simplex is equal to $1/d!$, while the volume of the corresponding unit- n -cube is 1.

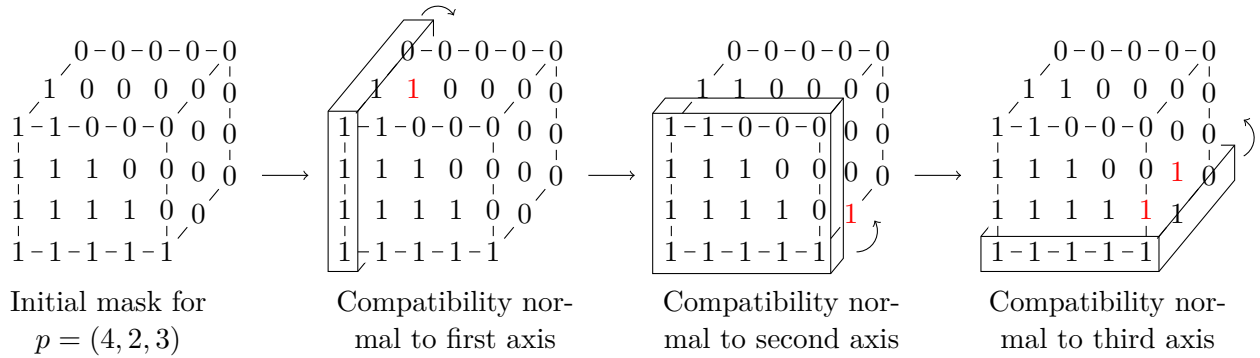


Figure 22. Construction of three-dimensional trunk space initial tensor-product masks.

Acknowledgements

We gratefully acknowledge the support of Deutsche Forschungsgemeinschaft (DFG) through the grant KO 4570/2-1 as well as project 414265976 – TRR 277 C-01. This publication was also made possible in part by the CSIRO Professorial Chair in Computational Geoscience at Curtin University and the Deep Earth Imaging Enterprise Future Science Platforms of the Commonwealth Scientific Industrial Research Organisation, CSIRO, of Australia. This project has received funding from the European Union’s Horizon 2020 research and innovation programme under the Marie Skłodowska-Curie grant agreement No 777778 (MATHROCKS). The Curtin Corrosion Centre and the Curtin Institute for Computation kindly provide ongoing support.

References

- [1] A. Düster, E. Rank, and B. Szabó, *The p -Version of the Finite Element and Finite Cell Methods*, pp. 1–35. 09 2017.
- [2] C. Schwab, *p - and hp - Finite Element Methods: Theory and Applications in Solid and Fluid Mechanics*. Numerical mathematics and scientific computation, Oxford University Press, 1998.
- [3] D. D’Angella, N. Zander, S. Kollmannsberger, F. Frischmann, E. Rank, A. Schröder, and A. Reali, “Multi-level hp -adaptivity and explicit error estimation,” *Advanced Modeling and Simulation in Engineering Sciences*, vol. 3, 12 2016.
- [4] V. Darrigrand, D. Pardo, T. Frelet, I. Gomez-Revuelto, and L. Garcia-Castillo, “A painless automatic hp -adaptive strategy for elliptic problems,” *Finite Elements in Analysis and Design*, vol. 178, p. 103424, 10 2020.
- [5] L. Demkowicz, J. Oden, W. Rachowicz, and O. Hardy, “Toward a universal h - p adaptive finite element strategy, part 1. constrained approximation and data structure,” *Computer Methods in Applied Mechanics and Engineering*, vol. 77, no. 1, pp. 79 – 112, 1989.
- [6] N. Zander, T. Bog, S. Kollmannsberger, D. Schillinger, and E. Rank, “Multi-level hp -adaptivity: high-order mesh adaptivity without the difficulties of constraining hanging nodes,” *Computational Mechanics*, vol. 55, pp. 499–517, Feb. 2015.
- [7] N. Zander, T. Bog, M. Elhaddad, F. Frischmann, S. Kollmannsberger, and E. Rank, “The multi-level hp -method for three-dimensional problems: Dynamically changing high-order mesh refinement with arbitrary hanging nodes,” *Computer Methods in Applied Mechanics and Engineering*, vol. 310, pp. 252–277, Oct. 2016.
- [8] P. Di Stolfo and A. Schröder, “ C^k and C^0 hp -finite elements on d -dimensional meshes with arbitrary hanging nodes,” *Finite Elements in Analysis and Design*, vol. 192, p. 103529, 09 2021.
- [9] C. Geuzaine and J.-F. Remacle, “Gmsh: a three-dimensional finite element mesh generator with built-in pre- and post-processing facilities,” *International Journal for Numerical Methods in Engineering*, vol. 79, pp. 1309 – 1331, 09 2009.
- [10] Y. Yu, J. Liu, and Y. Zhang, “Hexdom: Polycube-based hexahedral-dominant mesh generation,” 03 2021.
- [11] K. Voronin, “A parallel mesh generator in 3D/4D,” *Portland Institute for Computational Science Publications.*, vol. 11, 2018.
- [12] R. Sevilla, S. Mendez, and A. Huerta, “NURBS-enhanced finite element method (NEFEM),” *International Journal for Numerical Methods in Engineering*, vol. 76, pp. 56–83, 10 2008.
- [13] E. Burman, S. Claus, P. Hansbo, M. Larson, and A. Massing, “CutFEM: Discretizing geometry and partial differential equations,” *International Journal for Numerical Methods in Engineering*, vol. 104, 12 2014.
- [14] M. Paszynski, V. Calo, and D. Pardo, “A direct solver with reutilization of LU factorizations for h -adaptive finite element grids with point singularities,” *Computers & Mathematics with Applications*, vol. 65, 12 2012.